Volume 23
Number 3
21 January 2021
Pages 501–750

CrystEngComm

rsc.li/crystengcomm

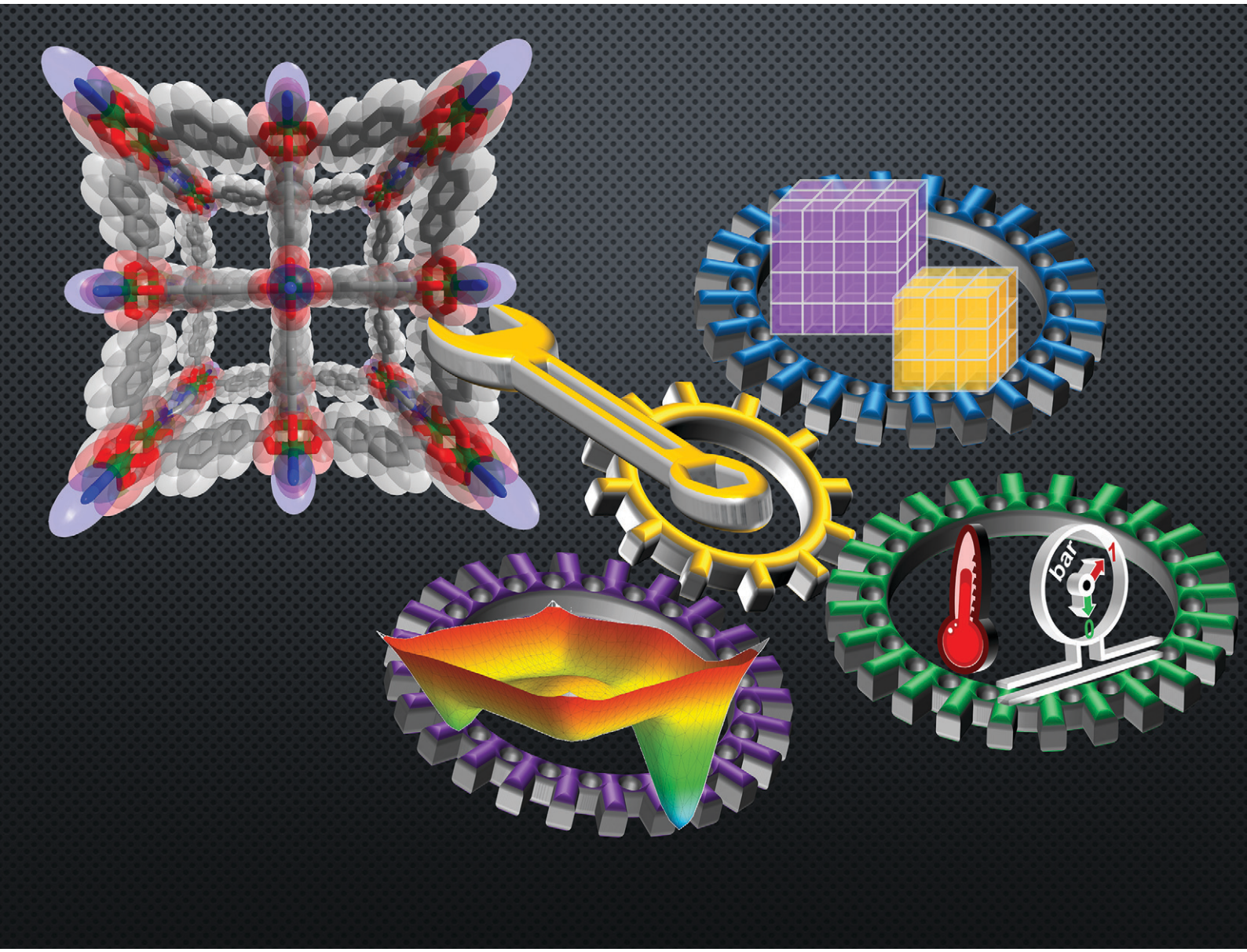

ISSN 1466-8033

ROYAL SOCIETY OF CHEMISTRY

PAPER

Irena Senkovska, Stefan Kaskel *et al.*
Tailoring adsorption induced switchability of a pillared layer MOF by crystal size engineering

CrystEngComm

PAPER

View Article Online
View Journal | View Issue

Cite this: *CrystEngComm*, 2021, **23**, 538

Tailoring adsorption induced switchability of a pillared layer MOF by crystal size engineering†

Leila Abylgazina, [a] Irena Senkovska, *[a] Sebastian Ehrling, [a] Volodymyr Bon, [a] Petko St. Petkov, [b] Jack D. Evans, [a] Svetlana Krylova, [c] Alexander Krylov [c] and Stefan Kaskel *[a]

The pillared layer framework DUT-8(Zn) (Zn_2(2,6-ndc)$_2$(dabco), 2,6-ndc = 2,6-naphthalenedicarboxylate, dabco = 1,4-diazabicyclo-[2.2.2]-octane, DUT = Dresden University of Technology) is a prototypical switchable MOF, showing characteristic adsorption and desorption induced open phase (op) to closed phase (cp) transformation associated with huge changes in cell volume. We demonstrate switchability strongly depends on a framework-specific critical particle size (d_{crit}). Superposed, the solvent removal process (pore desolvation stress contracting the framework) significantly controls the cp/op ratio after desolvation and, subsequently, the adsorption induced switchability characteristics of the system. After desolvation, the dense cp phase of DUT-8(Zn) shows no adsorption-induced reopening and therefore is non-porous for N_2 at 77 K and CO_2 at 195 K. However, polar molecules with a higher adsorption enthalpy, such as chloromethane at 249 K and dichloromethane (DCM) at 298 K can reopen the macro-sized crystals upon adsorption. For macro-sized particles, the outer surface energy is negligible and only the type of metal (Zn, Co, Ni) controls the DCM-induced gate opening pressure. The node hinge stiffness increases from Zn to Ni as confirmed by DFT calculations, X-ray crystal structural analysis, and low frequency Raman spectroscopy. This softer Zn-based node hinges and overall increased stabilization of cp *vs.* op phase shift the critical particle size at which switchability starts to become suppressed to even lower values (d_{crit} < 200 nm) as compared to the Ni-based system (d_{crit} ≈ 500 nm). Hence, the three factors affecting switchability (energetics of the empty host, (E_{op}–E_{cp}) (I), particle size (II), and desolvation stress (III)) appear to be of the same order of magnitude and should be considered collectively, not individually.

Received 13th October 2020,
Accepted 2nd November 2020

DOI: 10.1039/d0ce01497d

rsc.li/crystengcomm

Introduction

Switchable metal–organic frameworks or so-called soft porous crystals[1] demonstrate reversible dynamic transformations of the structure under the action of external stimuli such as guest elimination/reintroduction,[2] temperature,[3] pressure[4] or light.[5] Most frequently, the phase transition is triggered by adsorption or desorption of guest molecules and activation barriers lead to a hysteresis in the adsorption isotherm.[6] Due to their capability to undergo stimulated structural transformations, soft porous crystals are often discussed as materials with huge application potential in gas or liquid separation processes,[7] sensor technology,[8] and catalysis.[9] For the technological development of switchable MOFs in target applications, a fundamental understanding of the role of critical factors influencing and controlling framework switchability is of utmost importance and will provide a platform for tuning the switching characteristics.

One of the crucial factors affecting the switchability of MOFs is their structural composition as the metal clusters, organic linker and their connections can form softer or stiffer hinges. The impact of the metal nodes on the switchability of MOF has been previously discussed in the literature. For instance, switchability in the breathable MIL-53 series ([M(OH)(bdc)$_2$]$_n$ (M = Cr,[10] Al,[11] Fe,[12] Sc,[13] In,[14] Ga;[15] bdc = benzene-1,4-dicarboxylate) strongly depends on the metal centre. Pillared layer MOFs represent another class of porous coordination frameworks with representative switching

[a] *Chair of Inorganic Chemistry I, Technische Universität Dresden, Bergstrasse 66, 01069 Dresden, Germany. E-mail: irena.senkovska@tu-dresden.de, stefan.kaskel@tu-dresden.de*
[b] *Faculty of Chemistry and Pharmacy, University of Sofia, 1126, Sofia, Bulgaria*
[c] *Kirensky Institute of Physics, Federal Research Center KSC SB RAS, 660036 Krasnoyarsk, Russia*

† Electronic supplementary information (ESI) available: Rietveld plots, SEM images, thermogravimetric analysis, gas adsorption data, PXRD patterns, vapour adsorption data, heat of adsorption determination, crystallographic figures, IR spectra, Raman spectra, spin related cluster and framework optimization, simulated UV-vis spectra. CCDC 2020029 and 2020030. For ESI and crystallographic data in CIF or other electronic format see DOI: 10.1039/d0ce01497d

transitions.[16] DMOFs (dabco MOFs) with the composition $[M_2(bdc)_2(dabco)]_n$ (M = Zn,[17] Co,[18] Cu,[19] Ni[20]) demonstrate contractive/expansive behaviour during desolvation/resolvation. Structural response can be tuned by modification of linker chemical composition,[21] which leads to distinct breathing effects during adsorption of CO_2 at 195 K.[22]

In recent years, several publications appeared reporting the pivotal role of crystal size and morphology on the switchability.[23] Downsizing of flexible MOF crystallites to the nanoscale regime can alter their adsorption properties and even generate new intrinsic features differing from the bulk MOFs.[24–31] For example, the macrocrystals of the pillared layer compound $[Cu_2(bdc)_2(bipy)]_n$ (bipy = 4,4′-bipyridine) show an open pore (op) to closed pore (cp) structural transition upon guest desorption, while downsized crystals (1 μm) undergo the op to cp transition only after thermal treatment.[26]

The strong impact of the crystal or grain size on the switching characteristics of the "gate pressure" pillared layer MOF $[Ni_2(2,6\text{-ndc})_2dabco]_n$, also known as DUT-8(Ni)[32] (DUT = Dresden University of Technology) was revealed recently.[24] Small DUT-8(Ni) crystals (below 500 nm in size) do not undergo the op to cp transition upon desolvation.[24] The same behaviour is also characteristic for submicron-sized crystals of DUT-8(Co).[33] The macro-sized crystals of DUT-8(Co), however, do not show any responsivity to nitrogen (at 77 K) or carbon dioxide (at 195 K) during adsorption, in contrast to DUT-8(Ni), that shows pronounced switchability under the same conditions.[33] This suggests that the influences of particle size and metal node are interconnected and both aspects change the flexibility characteristics at a similar order of magnitude. Moreover, there may be more factors overlooked in the past, contributing to the phase transition energetics.

In the following, we present a detailed study of the adsorption induced switching of DUT-8(Zn).[34] In addition to the influence of the metal node and the particle size, we also demonstrate the influence of solvent molecules in the pores and the subsequent desolvation procedure on the framework response.

Experimental section

Analytical methods

Scanning electron microscopy (SEM). SEM measurements were carried out taking secondary electron using 2 kV acceleration voltage and a working distance of 14 mm on a SU8020 from Hitachi. Prior to the measurement the samples were sputtered with Au to enhance surface conductivity.

Powder X-ray diffraction (PXRD). (PXRD) patterns were obtained at room temperature on a STOE STADI P diffractometer using Cu-Kα_1 radiation (λ = 1.5406 Å) and a 2D detector (Mythen, Dectris). All measurements were performed in transmission geometry using a rotating flatbed sample holder, 2Θ resolution of 3.12° and exposition time of 120 s per step.

Nuclear magnetic resonance spectroscopy. ^{1}H NMR experiments in solution were performed using a Bruker AVANCE 300 MHz (300 MHz, 282 MHz) spectrometer The samples were dissolved in DCl/D_2O in DMSO-d6.

Elemental analysis. CHN analysis was performed on a EuroEA elemental Analyser.

Thermogravimetric analyses TGA. TGA were performed in synthetic air flow in a temperature range from 298 K to 1273 K with a heating rate of 5 K min^{-1} using a STA 409 PC from NETZSCH Company.

Physisorption. Volumetric physisorption experiments, nitrogen adsorption at 77 K, carbon dioxide at 195 K were performed on Autosorb IQ apparatus, using liquid nitrogen or a mixture of dry ice with isopropanol, respectively, to reach the temperatures of measurements. Helium, nitrogen, carbon dioxide with purity of 99.999% was used for all the experiments. Chloromethane adsorption at 249 K was measured on BELSORP-max apparatus equipped with cryostat.

Vapour adsorption of different solvents were performed using BELSORP-max apparatus at 298 K. Prior to the adsorption measurement the samples were evacuated at room temperature for 16 h, besides samples desolvated by means of supercritical carbon dioxide.

IR spectroscopy. FT-IR ATR spectra were collected at 2 cm^{-1} resolution ranging from 4000 to 400 cm^{-1} using a Bruker Vertex 70 alpha instrument equipped with an ATR accessory (diamond crystal) and placed inside the device.

Raman spectroscopy. Raman spectra in the 180° geometry were recorded at room temperature on a Horiba Jobin Yvon T64000 spectrometer equipped with a liquid nitrogen cooled charge coupled device detection system in subtractive dispersion mode. Ar^+ ion laser (Stabilite®2017, Spectra-Physics) with λ = 514.5 nm and Kr^+ ion laser (Lexel 95 K) with λ = 647.1 nm were used. The spectra were measured with the excitation power on the sample of 0.7 mW. The experiments were carried out using the incident laser beam focused on the sample by a 50× Olympus objective lens with a numerical aperture of 0.75. The scattered light was collected by the same objective lens and analysed through a polarizer and λ-plate. Spectroscopic measurements were performed in the subtractive dispersion mode, which attained a low-frequency limit of 10 cm^{-1} in the present setup, to investigate the low-frequency spectra. The deformation of the low-frequency spectral edge by an optical slit, which sometimes smears the true features of low-frequency spectra, was carefully eliminated by rigorous optical alignment.

Single crystal X-ray diffraction. A single crystal of as synthesized DUT-8(Zn) was prepared in a borosilicate glass capillary (d = 0.3 mm) with small amount of *N*,*N*-dimethylformadmide (DMF). The dataset was collected at MX BL14.2 beamline of BESSY II synchrotron, operated by

Helmholtz-Zentrum Berlin für Materialien und Energie.[35] Four images from different crystal orientations were collected in order to determine the crystal symmetry and scan range using iMosflm program.[36] The φ-scan with oscillation step of $\Delta\varphi$ = 1° was used for collection of 180 frames, which were processed automatically using XDSAPP 2.0 software.[37] The crystal structure was solved by direct methods and refined by full matrix least-squares on F^2 using SHELX-2018/3 program package.[38] All non-hydrogen atoms were refined in anisotropic approximation. Hydrogen atoms were refined in geometrically calculated positions using "riding model" with U_{iso}(H) = 1.2U_{iso}(C). Disordered guest molecules could not be refined unambiguously from the difference Fourier map, hence, SQUEEZE routine in PLATON was used to generate the reflection intensities with subtracted solvent contribution.[39] As a result, 679 electrons were squeezed from the volume of 2235 Å^3. CCDC-2020029 contains the supplementary crystallographic data for DUT-8(Zn)_op.

Crystal data for as made $[Zn_2(2,6\text{-ndc})_2(dabco)(DMF)_x]_n$ (**1**_op): $C_{30}H_{24}O_8N_2Zn_2$ (framework only, solvent molecules are omitted), M = 671.25 g mol^{-1}, monoclinic, $C2/m$ (No. 12), a = 19.000(4) Å, b = 18.070(4) Å c = 9.6700(19) Å, β = 95.87(3)°, V = 3302.6(11) Å^3, Z = 2, λ = 0.79990 Å, T = 296 K, θ_{max} = 29.996°, reflections/parameter 2895/106, R_{int} = 0.0988, R_1 = 0.1070, wR_2 = 0.3048, S = 1.131 largest diff. peak 1.536 e Å^{-3} and hole −1.445 e Å^3.

Structure solution and refinement of 1_cp phase from powder X-ray diffraction (PXRD) data. PXRD patterns of **1**_cp were collected on Empyrean-2 diffractometer (Panalytical) equipped with parallel linear Cu-Kα_1 beam (hybrid 2xGe(220) monochromator). 10 mm mask and primary divergence and secondary antiscatter slits with $\frac{1}{4}$° opening were used upon data collection. Pixcel-3D detector in 1D scanning mode (255 active channels) was used. The data collection was performed in transmission geometry using capillary spinner setup and the sample was sealed in the borosilicate capillary under argon. The measured PXRD was indexed using DICVOL91. The obtained unit cell parameters were similar to the cp phase of DUT-8(Ni),[40] therefore, the initial model for the Rietveld refinement was obtained by geometry optimization of the DUT-8(Ni) cp phase with unit cell parameters, derived from the *ab initio* indexing procedure. The Rietveld refinement with energy option (energy contribution 1%) was performed using reflex tool of Materials Studio 5.0 software package.[41] Zinc atoms, naphthalene cores, dabco ligands and carboxylates were treated as rigid bodies. The Rietveld plot is shown in Fig. S6 (ESI†). CCDC-2020030 contains the supplementary crystallographic data for DUT-8(Zn)_cp.

Crystal data for **1**_cp $[Zn_2(2,6\text{-ndc})_2(dabco)]_n$: $C_{30}H_{24}O_8N_2Zn_2$, M = 671.25 g mol^{-1}, triclinic, $P\bar{1}$ (No. 1), a = 7.1276(12) Å, b = 8.5505(13) Å, c = 13.1270(23) Å, α = 84.148(23)°, β = 116.032(19)°, γ = 108.462(16)°, V = 681.24(56) Å^3, Z = 1, λ = 1.54059 Å, T = 296 K, $2\theta_{range}$ = 5–70°, Profile function Thompson–Cox–Hastings, U = 0.4946, V = 0.0066, W = 0.00343, X = 0.4260, Y = 0.1735, refined motion groups/degree of freedom 9/45, R_p = 0.0547, R_{wp} = 0.0791.

***In situ* experiments.** *In situ* PXRD patterns upon physisorption of CH_3Cl at 249 K were measured at KMC-2 beamline of BESSY II synchrotron, operated by Helmholtz-Zentrum Berlin für Materialien und Energie.[42] An in house-developed automated instrumentation, based on the volumetric adsorption instrument and closed-cycle Helium cryostat, equipped with adsorption chamber with beryllium domes was used in all experiments.[43] PXRD patterns were measured at constant wavelength λ = 1.3332 Å (E = 9300 eV) in transmission geometry. Diffraction images were collected using 2θ scans and Vantec 2000 detector (Bruker). Each 2D image was measured with 31 s exposure. **1b** sample was used in experiment. In order to cut off reflections coming from the crystalline Be-dome, tungsten slits with 5 mm aperture were mounted on the detector cone. The obtained diffraction images were integrated using DATASQUEEZE 2.2.9 (ref. 25) with further processing in FITYK 0.9 software.[44] Adsorption equilibrium setting was defined as pressure change of 0.1% within 300 s.

In situ PXRD experiments on **3c** in parallel to CO_2 adsorption at 195 K were performed on a specialized Empyrean powder X-ray diffractometer (ω–2θ goniometer, K-alpha1 system) using a customized setup based on ARS DE-102 closed cycle helium cryostat, which assured isothermal conditions in the temperature range of 30–300 ± 0.1 K. The adsorption cell is based on 1.33″ CF-flange and covered with a Beryllium dome. The cell was connected to the low-pressure port of the BELSORP-max volumetric adsorption instrument. The TTL-trigger was used for establishing the communication between BELSORP-max and Empyrean software and ensure the measurement of adsorption isotherm and PXRD pattern data collection in fully automated mode. The diffraction experiments were performed using ω–2θ scans in transmission geometry in the range of 2θ = 2–50°. Parallel linear Cu-Kα_1 beam, generated by hybrid 2xGe(220) monochromator, 4 mm mask, and primary divergence and secondary antiscatter slits with $\frac{1}{4}$° opening were used upon data collection. Pixcel-3D detector in 1D scanning mode (255 active channels) was used. A complete adsorption–desorption physisorption isotherm of carbon dioxide at 195 K was measured on 8.9 mg of sample, statically fixed in the X-ray beam, and PXRD patterns were recorded after equilibration (0.1% of pressure change within 300 s) at selected points of the isotherm *in situ* by means of an automated dosing procedure of BELSORP-max.

Density functional theory (DFT) modelling. The periodic DFT calculations of DUT-8(Zn) were carried out using the QUICKSTEP module of CP2K[45] with a mixed Gaussian and plane waves basis set.[46] Periodic boundary conditions were applied in all three dimensions. The PBE exchange-correlation functional was used[47] with Goedecker–Teter–Hutter (GTH) pseudo-potentials.[48–50] The orbital transformation method was employed for efficient wave function optimization. Basis sets of DZVP quality were used with a grid cutoff 360 Ry for the geometry optimization and 300 Ry for the molecular dynamic simulations.[51] In all

calculations, Grimme's DFT-D3 dispersion correction was applied.[52]

Molecular DFT was used to investigate the stability of the paddle wheel unit. Constraining geometry optimisations were performed using the NWchem 6.3 software package[53] with the PBE0 functional[54] and a polarized triple-zeta basis set (def2-TZVP).[55] Tight convergence criteria were employed. Input files can be found in the data repository of J. D. Evans (https://github.com/jackevansadl/supp-data).

Materials

$Zn(NO_3)_2{\cdot}6H_2O$ (99%), 2,6-H_2ndc (99%), dabco (99%) were purchased from Sigma Aldrich. All solvents were at least of analytical grade, purchased from commercial suppliers and used without further purification.

MOF synthesis

An overview of all samples investigated is presented in Fig. 1.

Macro-sized particles, 1. The synthesis procedure of DUT-8(Zn) reported by Klein *et al.* in 2012 was slightly modified.[34] All chemicals were dissolved separately: $Zn(NO_3)_2{\cdot}6H_2O$ (312 mg, 1.05 mmol, 1.7 eq.) in 5 mL *N*,*N*-dimethylformadmide (DMF), 2,6-H_2ndc (227 mg, 1.05 mmol, 1.7 eq.) in 20 mL DMF and dabco (70 mg, 0.625 mmol, 1 eq.) in 5 mL DMF using ultrasound bath before mixing for 20 min. The three resulting solutions were slowly mixed and heated in an oven at 353 K for 15 min. After the pre-treatment, the precipitate is formed, which is then removed by centrifugation. The filtrate was placed into Pyrex tubes and tempered at 393 K for 48 hours. After cooling to room temperature (RT), the crystals were washed several times with DMF.

Micron-sized particles, 2. Crystal-downsizing was accomplished by supersaturation route, reported by Kavoosi *et al.* in 2017 for the synthesis of rigid DUT-8(Ni).[71] All chemicals were dissolved separately: $Zn(NO_3)_2{\cdot}6H_2O$ (446 mg, 1.5 mmol, 0.5 eq.) in 5 mL DMF, 2,6-H_2ndc (296 mg, 1.37 mmol, 0.5 eq.) in 20 mL DMF and dabco (336 mg, 3 mmol, 1 eq.) in 5 mL DMF using ultrasound bath before mixing for 20 min. A cloudy suspension was obtained after mixing of all chemicals, which was ultrasonicated for 60 min. The mother liquor was removed by centrifugation and the resulting particles were washed several times with DMF.

Submicron-sized particles, 3. Submicron-sized crystals were obtained by increasing dabco concentration (with respect to **1** and **2**), which ensures even more rapid nucleation. All chemicals were dissolved separately and heated to 353 K prior mixing. Typically, to the hot, clear 2,6-H_2ndc solution (296 mg, 1.37 mmol, 0.3 eq.) in 20 mL DMF, $Zn(NO_3)_2{\cdot}6H_2O$ (446 mg, 1.5 mmol, 0.3 eq.) in 5 ml DMF solution is added. Finally, dabco solution (504 mg, 4.5 mmol, 1 eq.) in 5 ml DMF is added whereby the mixture immediately turns cloudy. The resulting mixture was then treated in an ultrasonic bath for 30 min at 353 K. The mother liquor was removed by centrifugation and the resulting particles were washed several times with DMF.

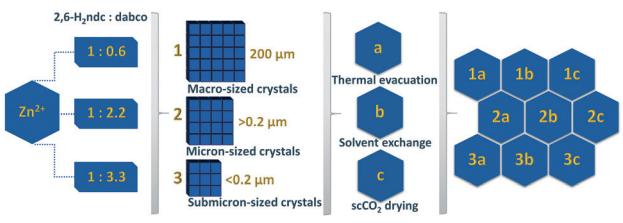

Fig. 1 Schematic overview of the DUT-8(Zn) samples synthesised using different precursor concentrations and desolvated under varying activation conditions.

Solvent removal procedure

The first activation procedure applied is the evacuation of the solvent used during the synthesis under reduced pressure at elevated temperature (procedure a). The samples were filtered in an argon flow and DMF was removed in dynamic vacuum at 423 K for 16 hours.

Alternatively, the DMF used in the synthesis was exchanged first by a lower boiling point solvent (DCM) during 3 days. Afterwards, it was removed in dynamic vacuum at 423 K for 16 hours (procedure b).

In the third procedure, using supercritical drying (SCD), DMF was exchanged with ethanol several times during 3 days.

The samples were desolvated by supercritical CO_2 drying technique, in which ethanol is exchanged with liquid CO_2 at high pressure (*i.e.*, >73 atm) during several hours. Afterwards, the sample is heated above the supercritical temperature of CO_2 (*i.e.*, 304 K). As a result, the framework is occupied by $scCO_2$, which is then slowly vented (procedure c).

1b: yield: 220 mg, 62% (based on Zn^{2+}). CHN analysis: $C_{30}H_{26}O_8N_2Zn_2$: calc.: C, 52.325%; H, 3.779%; N, 4.069%; found: C, 52.84%; H, 3.89%; N, 4.15%.

2b: yield 295 mg, 58% (based on Zn^{2+}). CHN analysis: $C_{30}H_{26}O_8N_2Zn_2$: C, 52.325%; H, 3.779%; N, 4.069%; found: C, 52.92%; H, 3.45%; N, 4.06%.

3c: yield: 350 mg, 69% (based on Zn^{2+}). CHN analysis: $C_{30}H_{26}O_8N_2Zn_2$: calc.: C, 52.325%; H, 3.779%; N, 4.069%; found: C, 49.63%; H, 4.21%; N, 3.95%.

Results and discussion

Crystal structure of open pore phase

To analyse the crystal structure, as made crystals were subjected to single-crystal X-ray analysis. The structure of DUT-8(Zn) was solved and refined in the monoclinic space group *C*2/*m*, which is different from the *P*4/*n* reported earlier from Rietveld refinement,[34] indicating conformational isomerism also in this compound, as discussed in detail for DUT-8(Ni).[56,57] As expected, the overall crystal structure is based on paddle wheel units, which are interconnected by 2,6-naphthalenedicarboxylates (2,6-ndc^{2-}) forming 2D layers, which are further linked by neutral dabco ligands to form a 3D framework with **pcu** underlying topology (Fig. 2). According to the crystallographic data, Zn···Zn distance in

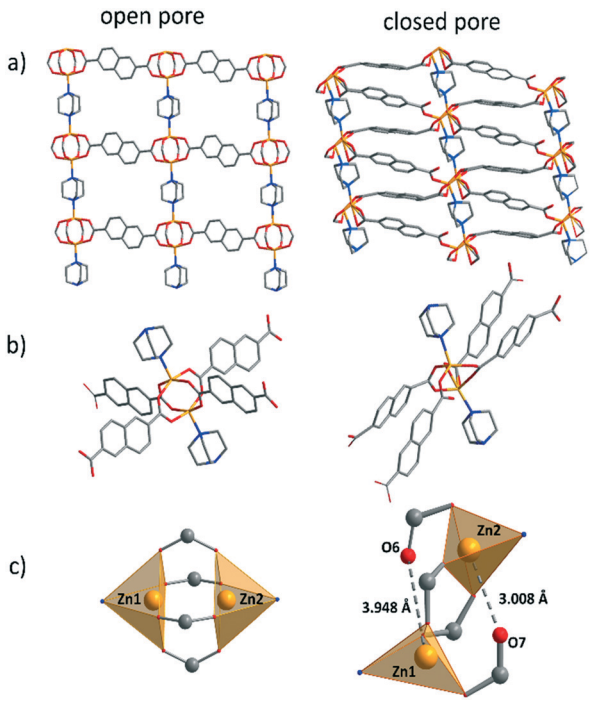

Fig. 2 Crystal structure of: a) **1**_op and **1**_cp along *b* direction; b) the coordination environment of the Zn paddle wheel unit in: **1**_op and **1**_cp; c) view on coordination polyhedron of **1**_op and **1**_cp. C – in grey, O – in red, N – in blue, Zn – in yellow. Hydrogen atoms are omitted for clarity.

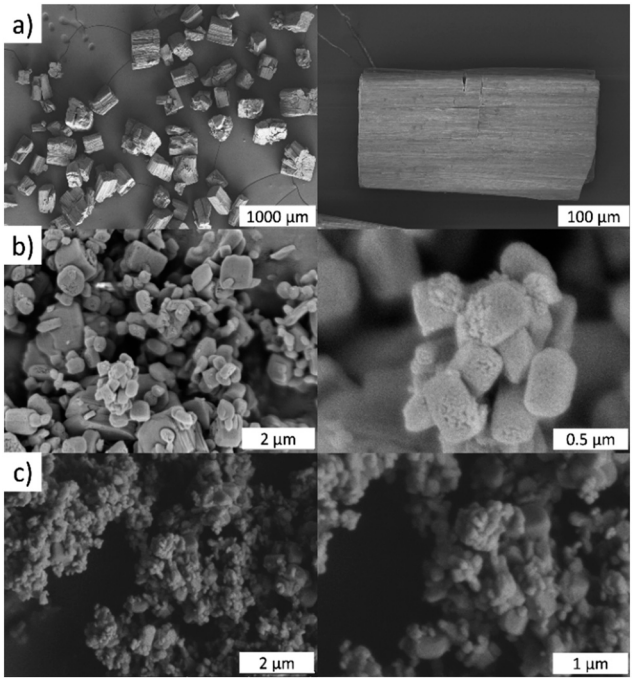

Fig. 3 SEM images of: a) macro-, b) micron-, c) submicron-sized particles of DUT-8(Zn).

1_op is 2.966 Å, which is significantly longer than in DUT-8(Ni) and DUT-8(Co) (2.653 and 2.691 Å).[33] The length of the Zn–N bond is 2.084 Å. The comparison of this value with corresponding M–N bond lengths in DUT-8(Ni) and DUT-8(Co), shows that the value in DUT-8(Zn) is in between. The Zn–Zn–N angle is 178.65°, and comparable with that observed in DUT-8(Ni) (177.59°) (Table S1, ESI†).[56]

Particle size

As we have reported for DUT-8(Ni) and DUT-8(Co), the switching characteristics are sensitive to crystal size distribution and it was also expected for DUT-8(Zn). Hence, DUT-8(Zn) was synthesized in three different size regimes: **1** – particles up to 200 µm (macro-sized); **2** – micron-sized particles (0.2–1 µm); and **3** – submicron-sized particles (<0.2 µm) (Fig. 3). As depicted, the average crystallite size of macro-sized system **1** is *ca.* 200 µm, whereas this value ranges from 0.2 to 1 µm for sample **2**. Sample **3** represents the smallest crystal size regime of 0.07–0.2 µm.

Powder X-ray diffraction (PXRD) patterns for all as-synthesized crystals are in good agreement with the pattern of DUT-8(Zn) calculated from the crystal structure (Fig. S1, ESI†), indicating that all samples are phase pure.

Thermal analysis

In order to estimate thermal stability of **1**–**3**, thermogravimetric analysis (TGA) was performed in synthetic air flow. Interestingly, the analysis discloses decreasing thermal stability with decreasing size of the crystals.

The decomposition of sample **1** starts at 673 K, whereas sample **2** starts to decompose at 653 K already (Fig. S2, ESI†). The decomposition proceeds in both samples in one step. Despite relatively small difference in average particle size between samples **2** and **3**, the thermal stability of sample **3** is considerably lower than for **2**, showing the first decomposition step starting from 493 K already, presumable associated with the dabco elimination.

Desolvation

The stress acting on the framework during desolvation depends on surface tension and capillary forces imposed on the structure by the liquid- to gas-phase transformation of included solvent molecules, which are high especially when the solvent has a high boiling point and/or high surface tension.[58] A common approach to reduce the stress is to exchange the solvent with a low-boiling-point/low-surface-tension solvent (these parameters tend to be correlated) prior to heating the sample under vacuum.[59] The most gentle desolvation approach is supercritical drying using carbon dioxide as a working fluid.[60] Depending on the guest molecules present in the pore and desolvation technique applied, the forces acting on the framework can be varied[61] and indirect information of the relative robustness of the network can be extracted.

Activation directly from DMF is mostly successful only for very robust structures. For fragile mesoporous compounds, however, which cannot sustain activation from (*N*,*N*-dimethylformadmide) DMF, dichloromethane (DCM) or *n*-heptane can be used to prevent framework collapse.[59]

In the flexible compounds, high stress acting during desolvation may contribute to structural contractions. In contrast to stiff systems, which show a framework collapse, switchable MOFs show an adaptive response *via* phase transformation.

For example, Brammer *et al.* showed that desolvation of $Me_2NH_2[In(abdc)_2]_n$ (SHF-61, abdc = 2-aminobenzene-1,4-dicarboxyliate) from two different solvents (chloroform or DMF/H_2O) leads to two polymorphic-activated forms with very different pore openings and markedly different gas-adsorption properties.[61] Removal of $CHCl_3$ leads to little change in the host framework, which exhibits a high porosity. Desolvation from DMF/H_2O leads to significant framework contraction and a low porosity phase. Interestingly, the framework contraction during desolvation of DMF/H_2O is continuous, and partial desolvation produces a partially contracted framework.

It should be mentioned, that in robust MOFs, the diffusion pathway for solvent removal are persistent for the whole activation period, ensuring the continuous movement of guests from the crystal inside to the surface. In flexible compounds, however, where pores are changing their geometry during solvent removal, the residence time of the solvent and the diffusion kinetics through the channels might play an additional crucial role in the activation process and should not be overlooked. The closing of the pores (first order phase transition) may lead to blockage of the diffusion pathways and retained regions with trapped solvent molecules. Therefore, one would expect, that solvents showing high interaction with the framework and possessing high boiling points (such as DMF) should also be more difficult to remove from a kinetic point of view.

In a first series, according to the procedure reported earlier,[34] the desolvation of the DUT-8(Zn) crystals was performed by direct removal of DMF (solvent used during the synthesis) in vacuum at 423 K (procedure a). DMF can be considered as a larger molecule among the solvents investigated here, with a kinetic diameter of 5.5 Å, and a very large dipole moment (3.8 D).[62] Therefore, both strong attractive interaction between MOF and DMF and slower diffusion rate should be expected.

The direct removal of DMF results in a mixture of closed pore (cp) and open pore (op) phases in the sample **1a** (Fig. 4), in agreement with results reported in 2012.[34] PXRD patterns of **2a** and **3a** indicate that the major part of the sample remains in the op phase with only an insignificant amount of cp phase. After activation, the samples were dissolved in DCl/D_2O and DMSO-d6 mixture, and subjected to NMR analysis to reveal residual DMF molecules in the framework (Fig. S3, ESI†).

In order to reduce the stress during solvent removal, DMF was exchanged with dichloromethane before desolvation under reduced pressure at 423 K during 16 h (procedure b). DCM is a molecule with a smaller kinetic diameter (4.70 Å),[63] smaller dipole moment (1.62 D)[64] and low boiling point (312.6 K), therefore, in comparison to DMF, it should be easier to remove. According to PXRD (Fig. 4), the desolvation of the macro-sized

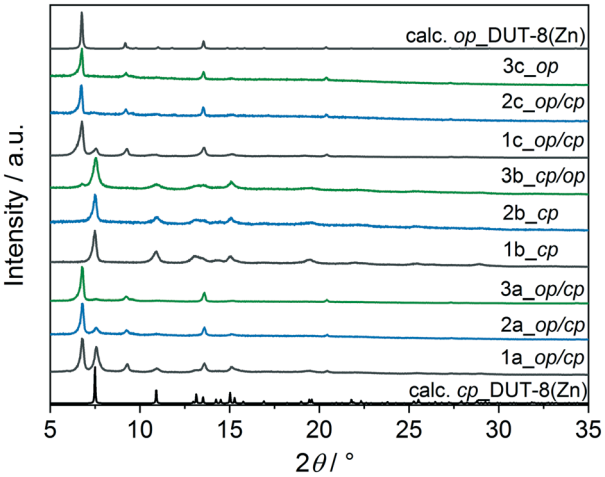

Fig. 4 PXRD patterns of **1**_macro-, **2**_micron-, **3**_submicron-sized particles of DUT-8(Zn) after different solvent removal procedures applied: (a) indicates desolvation from DMF in vacuum at 423 K, (b) indicates desolvation from DCM in vacuum at 423 K and (c) indicates desolvation using SCD. The calculated pattern of the op and cp phases DUT-8(Zn) are given for comparison.

1b and micron-sized crystals **2b** triggers the structural transformation from op to cp phase, in which the framework undergoes a significant shearing to minimize the amount of void space. The submicron-sized crystals **3b** show mainly the cp phase with a small amount of op phase.

To further reduce the stress on the framework, all samples were subjected to supercritical CO_2 drying after washing several times with ethanol (Fig. 4). In this case, the macro-sized particles **1c** yield a mixture of op and cp phases, the fraction of the cp phase in micron-sized particles **2c** is very small, and submicron-sized particles **3c** completely remain the original op phase, as observed for as-synthesized form. This indicates the robustness of the system under supercritical CO_2 activation conditions.

Comparing the structural response of DUT-8(Zn) towards different desolvation techniques, it may be hypothesized that the energy barrier for framework closing increases with decreasing particle size (Fig. 5). The small particles can rest in the metastable desolvated op state while the large particles transform into the thermodynamically preferable cp state. For $scCO_2$ the desorption stress is so small that the transformation of largest particles is incomplete. Contrastingly, the deformation stress of DCM is larger resulting in the smallest particles to transform almost completely.

The results of activation from DMF, however are rather unexpected. The surface tension and capillary forces are expected to be higher for DMF than for DCM and, therefore, support the closing, which is not the case. There are likely differences in the diffusion rates, which can also play a role.

Structure of the closed pore phase

Since the quality of the single crystals after solvent removal was not sufficient to collect a high quality dataset, a

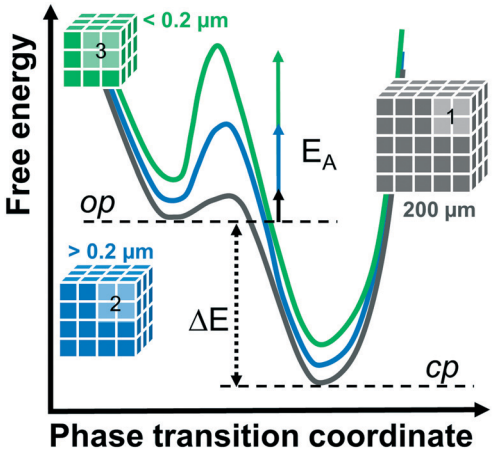

Fig. 5 Schematic representation of the energy diagrams for phase transitions from the op to cp phase depending on particle size.

structural model was refined against powder X-ray diffraction data in a triclinic space group (Fig. S4, ESI†). The main cluster deformation is reflected in the change of M···M and M–O distances. The Zn atoms move apart, resulting in a change of the Zn···Zn distance from 2.97 (in the op) to 3.80 Å (in the cp) (Table S1, ESI†), which leads to a strong elongation of some Zn–O bonds (Fig. 2). In the cause of that the coordination polyhedron changes from quadratic pyramidal to distorted tetrahedral, since two Zn–O bonds are disintegrated.[65]

Adsorption characteristics

Switching transformations from closed to open pore phases and *vice versa* induced by adsorption stimuli and their dependence on the crystal size was previously studied in isomorphous DUT-8(Ni) and DUT-8(Co) systems, revealing striking differences in adsorption behaviour, due to characteristic differences in framework's elastic response.[33] The underlying electronic differences, in case of Ni, Co and Zn should be reflected in closing/opening characteristics of respective MOFs. Indeed, the DUT-8(Zn) samples demonstrate pronounced differences in their adsorption isotherms compared to the Co and Ni analogues. Since the solvent removal techniques described above produce samples with varying ratio of op/cp phases, and the exact ratio is difficult to extract from PXRD patterns, we evaluated the porosity and structural response of all samples by means of adsorption of nitrogen at 77 K, carbon dioxide at 195 K, and chloromethanes at 249–298 K.

Samples desolvated from DMF (a).[33] The obtained N_2 (77 K) physisorption isotherms can be classified as type Ia, characteristic for microporous rigid materials (Fig. 6a). The maximum nitrogen uptake follows the trend expected from XRD data, where samples with higher amount of the op phase show the highest uptake and *vice versa* (Fig. 8). The cp fraction remains in the cp state and is not responsive to nitrogen over the entire pressure range.

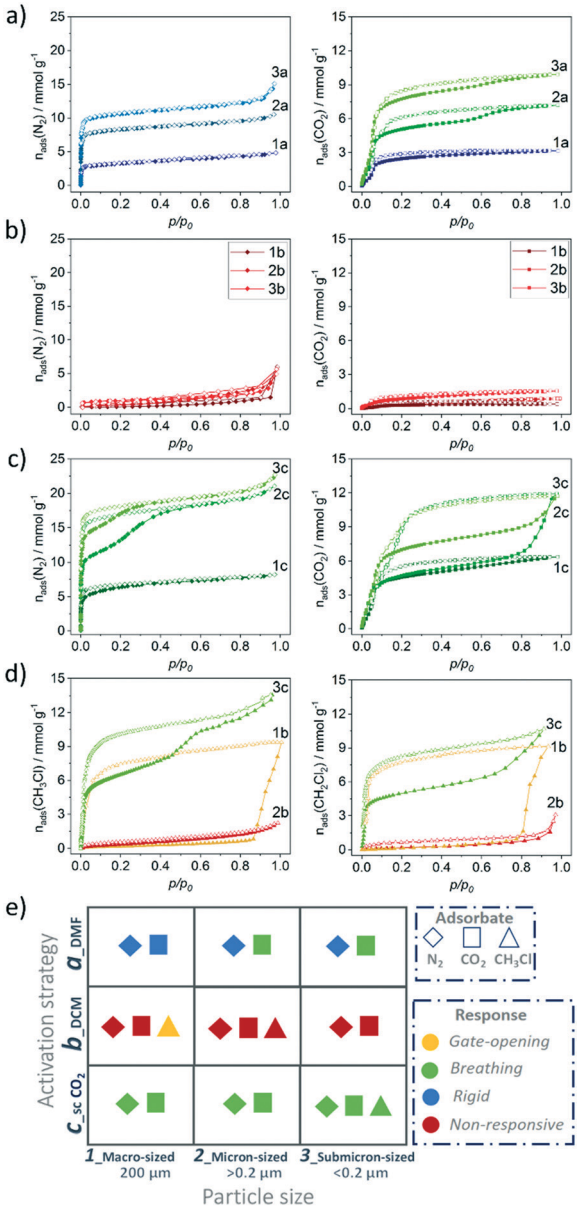

Fig. 6 Nitrogen at 77 K and carbon dioxide physisorption at 195 K on: a) samples **1a**, **2a**, **3a** activated from DMF; b) samples **1b**, **2b**, **3b** activated from DCM; c) samples **1c**, **2c**, **3c** activated *via* SCD; d) chloromethane at 249 K and dichloromethane adsorption at 298 K on samples **1b**, **2b**, **3c**; e) summary of structural response upon adsorption depending on particle size and activation strategy.

The adsorption of CO_2 at 195 K (Fig. 6a and 8), a guest with higher adsorption enthalpy, demonstrates some structural dynamics. However, the presence of mixed phases in the samples makes it difficult to interpret the data. The XRD patterns collected after adsorption reveal a slightly increased amount of the cp phase in comparison to the samples before experiments in case of **2a** and **3a**. This fact is pointing toward a possible breathing mechanism of the op phase during the adsorption/desorption cycle (Fig. S5, ESI).†

Samples desolvated from DCM (b). Analysis of PXRD patterns of the samples desolvated from DCM shows a

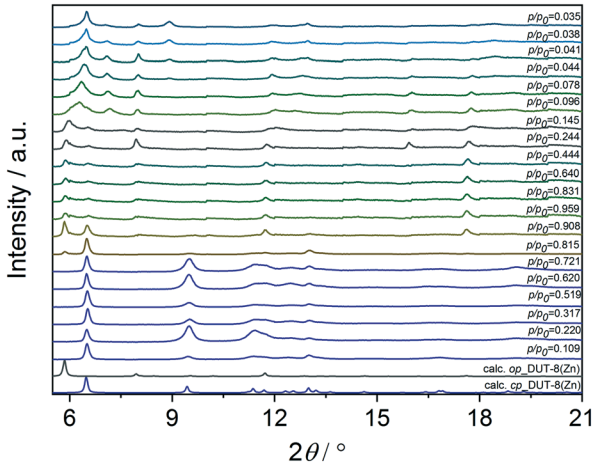

Fig. 7 *In situ* PXRD measured on **1b** during adsorption of chloromethane on DUT-8(Zn) at 249 K.

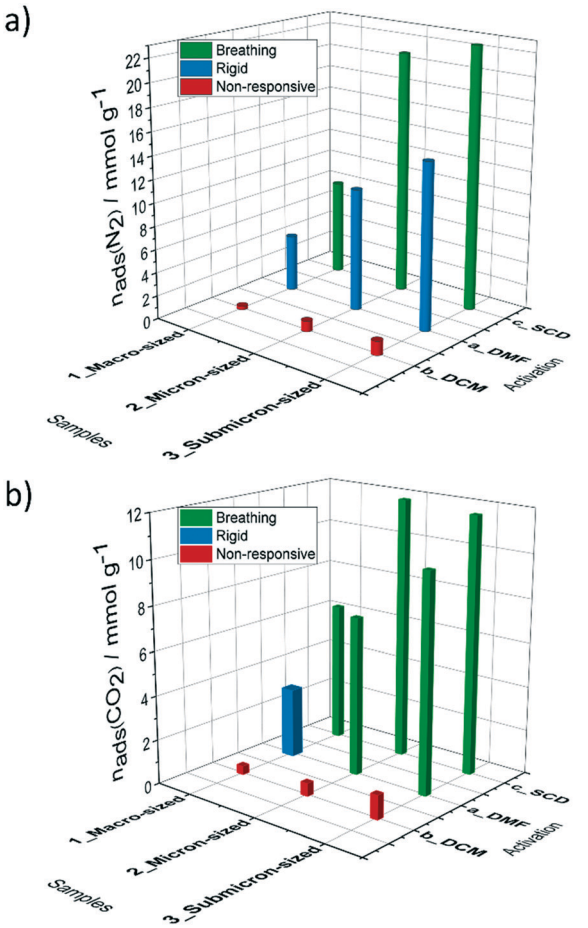

Fig. 8 Comparison of a) nitrogen (77 K) and b) carbon dioxide (195 K) uptake and structural response depending on particle size and activation strategy.

transition to the cp phase upon activation (Fig. 4). The N_2 and CO_2 physisorption isotherms show low uptake, indicating the high stability of the cp phase under these conditions (Fig. 6b and 8). However, more polar, small molecules, such as chloromethane at 249 K and dichloromethane at 298 K (kinetic diameters 4.05 and 4.70 Å, respectively)[66] are able to provoke structural transition in macro-sized particles **1**. The isotherms are characterized by typical gate opening shape with a gate opening relative pressure of 0.87 and 0.80, respectively. More interesting, the chloromethanes can discriminate between the particles of different size. The isotherms of micron-sized particles **2b** display no structural changes (Fig. 6d). This observation clearly shows, that the decreasing particle size, and associated increase in outer surface area and surface energy adds to the energy barrier of cp–op phase transformation.[67]

To analyse the structural phases induced by CH_3Cl adsorption, parallelised adsorption/diffraction experiments were performed on sample **1b** at KMC-2 beamline of BESSY II synchrotron (Fig. 7 and S6 ESI†). In the pre-gate region of the isotherm, the analysis of the PXRDs indicated the existence of pure cp phase. At p/p_0 = 0.815 the pattern indicates a first order transition of the structure from nonporous cp to porous op phase without appearance of any intermediate phases. PXRD patterns measured at saturation at p/p_0 = 0.959 (the highest pressure reached) and upon desorption of chloromethane until "gate closing" show coexistence of cp and op phases. The intensity of reflections belonging to op phase is strongly influenced by strong absorption and diffuse scattering, attributed to adsorbed chloromethane.

The effect is nicely seen in the PXRDs measured upon "gate closing" at p/p_0 between 0.14 and 0.24, in which reduction of CH_3Cl amount in the pores significantly increases the intensity of the op phase reflections.

Further desorption of the CH_3Cl from the pores induces a phase transition to an intermediate phase (ip) in the range of p/p_0 = 0.09–0.03.

The first reflection at 2θ = 6.5° could correspond to the cp phase, however a few additional reflections appear at 2θ = 7.05, 8.05 and 8.95° that are not attributed to op or cp phases. However, severe peak broadening and limited number of reflections hinders quantitative analysis of the PXRD patterns. In contrast to CH_2Cl_2, $CHCl_3$ and CCl_4 are unable to initiate the switching for **2b** or for **1b** at 298 K (Fig. S7, ESI†). The adsorption enthalpies for $CHCl_3$ and CCl_4 may be expected to be higher, than for CH_3Cl and CH_2Cl_2. However, as the size differs considerably, significant differences in maximal loadings per formula unit of MOF (n_{max}) can be estimated (Table 1).[63]

Hence, the total adsorption energy ($n_{max} \cdot E_{ads}$) per Zn_2(2,6-ndc)$_2$dabco formula unit (fu) of MOF decreases continuously from chloromethane to tetrachloromethane (Tab. 1). This provides an energetic reason for the absence of structural response $CHCl_3$ and CCl_4. In addition, the smaller kinetic diameter also favours adsorption kinetics and a reduced activation barrier can be expected to be lower for CH_3Cl and CH_2Cl_2.

Samples desolvated supercritically (c). All SCD samples, prior to adsorption contain predominantly the op phase. The

Table 1 Chloromethane characteristics[63]

Adsorptive	Kinetic diameter[a]/Å	n_{max}/mol fu^{-1}	E_{ads}/kJ mol^{-1}	n_{max}·E_{ads}/kJ fu^{-1}
CCl_4	5.83	7	62	434
$CHCl_3$	5.47	9	57	513
CH_2Cl_2	4.70	11	51	561
CH_3Cl	4.05	19	36	684

E_{ads} – adsorption energy at 300 K. [a] Kinetic diameters are given as Lennard-Jones parameters taken from ref. 66.

physisorption of N_2 at 77 K, CO_2 at 195 K, chloromethane at 249 K, and dichloromethane at 298 K reveal the flexible behaviour of the samples (breathing), since stepwise isotherms with hysteresis were observed. The flexible structural response (the hysteresis width) and uptake vary significantly with the particle size (Fig. 6c and 8).

In order to provide insight into this breathing mechanism, *in situ* experiments were performed during CO_2 adsorption at 195 K on SCD submicron-sized sample **3c** (Fig. S8, ESI†). Micropore filling occurs at low relative pressure. Starting from p/p_0 = 0.128 in the adsorption branch, the small additional peaks appear in the PXRD patterns, that are attributed to formation of the cp phase. The cp phase is visible in the *in situ* data in all patterns collected at relative pressures higher than 0.128 and in desorption branch, up to p/p_0 = 0.061.

At the last point measured at p/p_0 = 0.009, some residual amount of the cp phase is present. We can conclude, that during the adsorption of carbon dioxide, breathing of the structure occurs, suggesting a more labile paddle wheel is present, in comparison to the Ni and Co analogues that show type I adsorption isotherm without any signs of switchability.[33] An important observation is that the critical size for DUT-8(Zn), which suppress switchability is considerably smaller (<200 nm), compared to DUT-8(Ni) (<500 nm) and DUT-8(Co).[33] In addition, reduced desorption stress is needed, since the pure op phase could be achieved only by SCD activation. In contrast, the submicron-sized particles of DUT-8(Ni) and DUT-8(Co) withstand the removal of DCM under vacuum.

Spectroscopic investigations

Raman spectroscopy. It was already shown, that Raman spectroscopy is a powerful tool to reveal the differences in switchability of the frameworks due to the differences in the lattice vibration frequencies.[68]

In order to characterize the open pore phase, "as made" samples of DUT-8(Zn) in DMF were investigated first.

The characteristic band appears at 23 cm^{-1} for macro-sized sample (Fig. S9a, ESI†). The obtained characteristic lattice vibration bands values for DUT-8(Zn), DUT-8(Ni) and DUT-8(Co) are almost the same.[33,68]

The desolvated sample **1b** in the closed pore form were analysed, demonstrating two bands at 25.9 and 44.3 cm^{-1} (Fig. 9 and S9b, ESI†). The appearance of the second lattice vibration mode in the spectrum is obviously attributed to the drastic changes in the environment of the Zn atoms in the cp state, facilitating additional vibration modes of the framework constituents.

The decrease in frequency for the closed pore phase from 59.3 and 46.6 cm^{-1} for DUT-8(Ni) and DUT-8(Co), respectively, to 44.3 cm^{-1} for DUT-8(Zn) indicates that the force constant for DUT-8(Zn) cp framework is lower compared to Co. However, the difference between Co and Ni (4 cm^{-1}) is more pronounced as for Co and Zn (2 cm^{-1}).

Interestingly, the differences in the force constants are directly reflected in the gate opening pressure (p_{go}) upon DCM adsorption.

The closed pore phase of DUT-8(Ni), characterized by the highest force constant in the Ni, Co, Zn series, show the opening at *ca.* 9 kPa and the Co based variant at 34 kPa (difference of 25 kPa) (Fig. S10, ESI†). The p_{go} for cp phase of DUT-8(Zn) shifts to 44 kPa (difference between Co and Zn of 10 kPa), showing a systematic relation between the difference in the position of the peak in the Raman spectra and differences in relative gate opening pressure in DCM adsorption at 298 K.

IR-spectroscopy. The asymmetric stretching vibrations of the carboxylate in the recorded range are not influenced by the structural transition. For both compounds in the cp phases **1b** and **2b** the bands are at 1602 cm^{-1} and in the op

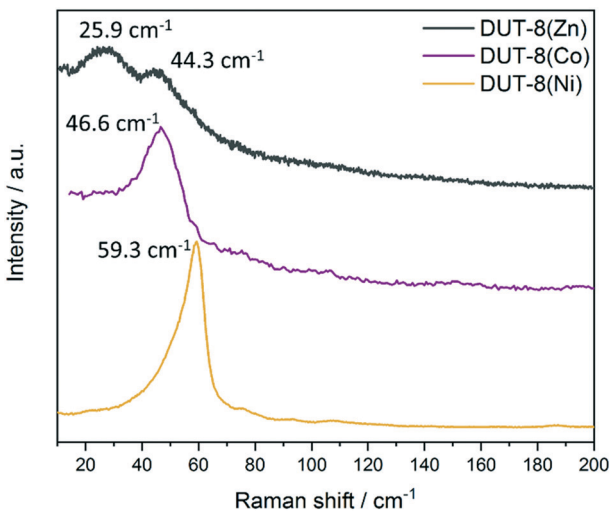

Fig. 9 The low frequency of Raman spectra of desolvated sample **1b** DUT-8(Zn) in comparison with DUT-8(Ni) and DUT-8(Co).

phase (**3c**) at 1605 cm^{-1} (Table S2, Fig. S11a, ESI†). The symmetric stretching for both compounds in the cp phase is at 1467 cm^{-1} and 1465 cm^{-1} in the op phase.

Furthermore, it is observed that the scissor deformation ($\delta(COO)_{oop}$) is slightly affected by the present phase.

In the cp phase the vibration can be observed at 806 cm^{-1} and in the op phase at 813 cm^{-1}. No differences were found in asymmetric vibrations of the dabco molecule in **2b** and **3c** (1057 cm^{-1} for op and cp phases).

Comparing the spectra of the cp phases of DUT-8(Ni), DUT-8(Co) and DUT-(Zn) (Fig. S11b and c, ESI†), one can see, that despite the stronger cluster deformation observed from crystallographic data for DUT-8(Zn) compound, the vibrations of the carboxylates (COO^-) in the recorded range are not significantly influenced, *i.e.* the asymmetric stretching vibration is at 1602 cm^{-1}, the symmetric stretching at 1467 cm^{-1}. The scissor deformation is more affected, since this appears at 816 cm^{-1} for Ni, at 802 cm^{-1} for Co and at 806 cm^{-1} for Zn.

Asymmetric vibrations are not influenced by metal node (1056 cm^{-1} for all compounds). The symmetric stretching vibrations of NC_3 are sensitive to metal and the positions of the bands differ (Zn: 779 cm^{-1}, Co: 776 cm^{-1}, Ni: 769 cm^{-1}, Fig. S11b and c, ESI†).

DFT simulations

First, atomistic simulation was applied to the paddle wheel unit to capture the behaviour of the molecular hinge present in the frameworks. Constrained geometric optimisations of a representative paddle wheel were performed, where the N–Zn–Zn and Zn–Zn–N angles were fixed and subsequently scanned for angles between 180° and 150° (Table S3, ESI†). In contrast to the previous reports for Ni, Co and combination of both metals in the paddle wheel,[33,69] the minimum energy configuration for the Zn paddle wheel is observed at 180°. Deformation of this unit to angles associated with the cp phase (approx. 155°) did not produce decomposition of the paddle wheel and requires almost 6 kJ mol^{-1}. This apparent rigidity of the Zn paddle wheel unit in the op phase is not reflected experimentally, suggesting that framework interactions and a more complex deformation mode are required to reproduce the transitions present in DUT-8(Zn).

The geometry of DUT-8(Zn) in the op and the cp phase was subject to energy minimization in periodic boundary conditions, using a unit cell of one Zn paddle wheel (PW) unit, two 2,6-ndc ligands, and one dabco pillar. During the energy minimization the cell shape, volume, and atomic positions were relaxed. The geometry of the cp phase was obtained starting from op phase after NPT MD simulation at 300 K and 1 atm pressure. The MD simulation performed in a fully flexible cell resulted in spontaneous op–cp transformation of the DUT-8(Zn) in 2 ps. Key interatomic distances and angles for op and cp phase are collected in Table S4.† We observe good agreement between the experimental and calculated geometry parameters. The calculated interatomic distances show, in line with experimental data, that upon closure the Zn paddle wheel undergoes significant structural deformation in comparison to DUT-8(Ni) and DUT-8(Co).[33] The Zn···Zn distance elongates by 0.97 Å, from 2.82 in op to 3.79 in the cp phase. Another notable deformation in the Zn PW is the Zn–O distances. From the analysis of the MD trajectories (Fig. S13b, ESI†) is visible that two of the total eight Zn–O distances in the Zn-PW are significantly elongated upon closure. In the minimized geometry of the cp phase, two Zn–O distances are elongated up to 3.78 and 3.61 Å, while the other six Zn–O distances are much smaller affected, 2.01–2.11 Å. Such deformation in the Zn-PW is responsible for the much smaller strain in the closed phase in comparison to DUT-8(Ni). The strain energy for DUT-8(Ni), where the Ni-PW stays intact upon closure, was calculated to be +102 kJ mol^{-1}, while for DUT-8(Zn) it is +78 kJ mol^{-1} (Table S5†) due to the Zn-PW partial distortion. On the other hand, the contribution from the dispersion interaction between 2,6-ndc linkers is very similar for DUT-8(Ni) and DUT-8(Zn), −188 kJ mol^{-1}, and −181 kJ mol^{-1}, respectively, leading overall to a higher stabilization of the cp *vs.* op phase for DUT-8(Zn) (−104 kJ mol^{-1}) in comparison with DUT-8(Ni) (−86 kJ mol^{-1}). These findings suggest that framework dynamics for DUT-8(Zn) and DUT-8(Ni) are dominated by the strain in the framework related to the stiffness of the paddle wheel hinge.

Summary

The critical particle size suppressing switchability in soft porous crystals is not identical for all MOFs but depends on the stiffness of the deforming building blocks, in case of DUT-8(M), the chemical composition of the paddle wheel hinges. For DUT-8(Zn), the smaller strain energy of the node results in a magnitude higher energy difference of the empty op and cp hosts ($\Delta E = E_{op} - E_{cp}$), as compared to DUT-8(Ni), resulting in a smaller critical particle size (higher surface energy) required to suppress switchability. This was demonstrated by studying particles of three size regimes: larger than 200 μm (macro-sized), in the range of 0.2–1 μm (micron-sized) and smaller than 0.20 μm (submicron-sized).

Crystallites of different size regimes behave also differently upon removal of the guest molecules. Removal of dichloromethane in vacuum at elevated temperature causes high desorption stress favouring the formation of thermodynamically stable phases as the phase transition to the closed pore phase is observed for macro- and micron-sized particles, whereas only for submicron-sized particles a mixture of cp/op phases was obtained. The application of mild supercritical drying favours the formation of metastable op phases: the macro-sized particles show a phase mixture of op and cp phases, whereas the micron and submicron sized particles remain in the metastable open pore phase.

The dense cp phase of DUT-8(Zn) shows no adsorption-induced pore opening for N_2 at 77 K and CO_2 at 195 K. The higher interaction energies of chloromethane at 249 K and dichloromethane at 298 K allow reopening of the macro-sized crystals upon adsorption, but not the smaller particles. This could indicate an intermediate particle size regime, in which the crystals close as monodomain crystals, without twinning, hence the lack of defects may be responsible for the barrier to reopen the structure.[24,70]

For macro-sized particles with negligible surface energy the influence of metal in the Ni, Co, Zn series (and associated differences in the softness of the paddle wheel in the cp phase) are clearly detected in the adsorption of DCM. The gate opening pressure shifts to the higher values from Ni to Zn, showing a growing kinetic barrier, the softening of the framework in the cp state and higher energy difference between op and cp structures.

Conflicts of interest

There are no conflicts to declare.

Acknowledgements

The authors thank the DFG (FOR 2433 MOF Switches, Project No. 279409724) for financial support. P.P. and J. D. E. thank Center for Information Services and High Performance Computing (ZIH) at TU Dresden for providing high-performance computing facilities. Authors acknowledge Helmholtz-Zentrum Berlin für Materialien und Energie for allocated beamtime at KMC-2 and MX14.2 beamlines. J. D. E. acknowledges the support of the Alexander von Humboldt foundation and HPC platforms provided by a GENCI grant (A0070807069).

References

1 S. Horike, S. Shimomura and S. Kitagawa, *Nat. Chem.*, 2009, **1**, 695.
2 S. K. Elsaidi, M. H. Mohamed, D. Banerjee and P. K. Thallapally, *Coord. Chem. Rev.*, 2018, **358**, 125.
3 A. Boutin, D. Bousquet, A. U. Ortiz, F.-X. Coudert, A. H. Fuchs, A. Ballandras, G. Weber, I. Bezverkhyy, J.-P. Bellat, G. Ortiz, G. Chaplais, J.-L. Paillaud, C. Marichal, H. Nouali and J. Patarin, *J. Phys. Chem. C*, 2013, **117**, 8180.
4 J. Wieme, S. M. J. Rogge, P. G. Yot, L. Vanduyfhuys, S.-K. Lee, J.-S. Chang, M. Waroquier, G. Maurin and V. Van Speybroeck, *J. Mater. Chem. A*, 2019, **7**, 22663.
5 R. Lyndon, K. Konstas, B. P. Ladewig, P. D. Southon, P. C. J. Kepert and M. R. Hill, *Angew. Chem., Int. Ed.*, 2013, **52**, 3695.
6 S. Krause, N. Hosono and S. Kitagawa, *Angew. Chem., Int. Ed.*, 2020, **59**, 15325.
7 Z. Chang, D. H. Yang, J. Xu, T. L. Hu and X. H. Bu, *Adv. Mater.*, 2015, **27**, 5432.
8 A. Chidambaram and K. C. Stylianou, *Inorg. Chem. Front.*, 2018, **5**, 979.
9 D. Yang and B. C. Gates, *ACS Catal.*, 2019, **9**, 1779.
10 F. Millange, C. Serre and G. Férey, *Chem. Commun.*, 2002, 822.
11 T. Loiseau, C. Serre, C. Huguenard, G. Fink, F. Taulelle, M. Henry, T. Bataille and G. Férey, *Chem. – Eur. J.*, 2004, **10**, 1373.
12 F. Millange, N. Guillou, R. I. Walton, J.-M. Grenèche, I. Margiolaki and G. Férey, *Chem. Commun.*, 2008, 4732.
13 J. P. S. Mowat, V. R. Seymour, J. M. Griffin, S. P. Thompson, A. M. Z. Slawin, D. Fairen-Jimenez, T. Düren, S. E. Ashbrook and P. A. Wright, *Dalton Trans.*, 2012, **41**, 3937.
14 E. V. Anokhina, M. Vougo-Zanda, X. Wang and A. J. Jacobson, *J. Am. Chem. Soc.*, 2005, **127**, 15000.
15 C. Volkringer, T. Loiseau, N. Guillou, G. Férey, E. Elkaïm and A. Vimont, *Dalton Trans.*, 2009, 2241.
16 F. ZareKarizi, M. Joharian and A. Morsali, *J. Mater. Chem. A*, 2018, **6**, 19288.
17 D. N. Dybtsev, H. Chun and K. Kim, *Angew. Chem., Int. Ed.*, 2004, **43**, 5033.
18 H. Wang, J. Getzschmann, I. Senkovska and S. Kaskel, *Microporous Mesoporous Mater.*, 2008, **116**, 653.
19 K. Seki and J. B. W. Mori, *J. Phys. Chem. B*, 2002, **106**, 1380.
20 P. Maniam and N. Stock, *Inorg. Chem.*, 2011, **50**, 5085.
21 S. Henke, A. Schneemann and R. A. Fischer, *Adv. Funct. Mater.*, 2013, **23**, 5990.
22 S. Henke, A. Schneemann, A. Wütscher and R. A. Fischer, *J. Am. Chem. Soc.*, 2012, **134**, 9464.
23 S. Furukawa, J. Reboul, S. Diring, K. Sumida and S. Kitagawa, *Chem. Soc. Rev.*, 2014, **43**, 5700.
24 H. Miura, V. Bon, I. Senkovska, S. Ehrling, S. Watanabe, M. Ohba and S. Kaskel, *Dalton Trans.*, 2017, **46**, 14002.
25 S. Krause, V. Bon, I. Senkovska, D. M. Többens, D. Wallacher, R. S. Pillai, G. Maurin and S. Kaskel, *Nat. Commun.*, 2018, **9**, 1573.
26 Y. Sakata, S. Furukawa, M. Kondo, K. Hirai, N. Horike, Y. Takashima, H. Uehara, N. Louvain, M. Meilikhov, T. Tsuruoka, S. Isoda, W. Kosaka, O. Sakata and S. Kitagawa, *Science*, 2013, **339**, 193.
27 X. Cheng, A. Zhang, K. Hou, M. Liu, Y. Wang, C. Song, G. Zhang and X. Guo, *Dalton Trans.*, 2013, **42**, 13698.
28 T. Omiya, K. Sasaki, Y. Uchida and N. Nishiyama, *ACS Appl. Nano Mater.*, 2018, **1**, 3779.
29 S. Tanaka, K. Fujita, Y. Miyake, M. Miyamoto, Y. Hasegawa, T. Makino, S. Van der Perre, J. Cousin Saint Remi, T. Van Assche, G. V. Baron and J. F. M. Denayer, *J. Phys. Chem. C*, 2015, **119**, 28430.
30 T. Tian, M. T. Wharmby, J. B. Parra, C. O. Ania and D. Fairen-Jimenez, *Dalton Trans.*, 2016, **45**, 6893.
31 S. Krause, V. Bon, H. Du, R. E. Dunin-Borkowski, U. Stoeck, I. Senkovska and S. Kaskel, *Beilstein J. Nanotechnol.*, 2019, **10**, 1737.
32 N. Klein, C. Herzog, M. Sabo, I. Senkovska, J. Getzschmann, S. Paasch, M. R. Lohe, E. Brunner and S. Kaskel, *Phys. Chem. Chem. Phys.*, 2010, **12**, 11778.
33 S. Ehrling, I. Senkovska, V. Bon, J. D. Evans, P. Petkov, Y. Krupskaya, V. Kataev, T. Wulf, A. Krylov, A. Vtyurin, S. Krylova, S. Adichtchev, E. Slyusareva, M. S. Weiss, B.

Büchner, T. Heine and S. Kaskel, *J. Mater. Chem. A*, 2019, **7**, 21459.
34 N. Klein, H. C. Hoffmann, A. Cadiau, J. Getzschmann, M. R. Lohe, S. Paasch, T. Heydenreich, K. Adil, I. Senkovska, E. Brunner and S. Kaskel, *J. Mater. Chem.*, 2012, **22**, 10303–10312.
35 U. Mueller, R. Förster, M. Hellmig, F. U. Huschmann, A. Kastner, P. Malecki, S. Pühringer, M. Röwer, K. Sparta, M. Steffien, M. Ühlein, P. Wilk and M. S. Weiss, *Eur. Phys. J. Plus*, 2015, **130**, 141.
36 T. G. G. Battye, L. Kontogiannis, O. Johnson, H. R. Powell and A. G. W. Leslie, *Acta Crystallogr., Sect. D: Biol. Crystallogr.*, 2011, **67**, 271.
37 K. M. Sparta, M. Krug, U. Heinemann, U. Mueller and M. S. Weiss, *J. Appl. Crystallogr.*, 2016, **49**, 1085.
38 G. Sheldrick, *Acta Crystallogr., Sect. C: Struct. Chem.*, 2015, **71**, 3.
39 A. Spek, *Acta Crystallogr., Sect. C: Struct. Chem.*, 2015, **71**, 9.
40 V. Bon, N. Klein, I. Senkovska, A. Heerwig, J. Getzschmann, D. Wallacher, I. Zizak, M. Brzhezinskaya, U. Mueller and S. Kaskel, *Phys. Chem. Chem. Phys.*, 2015, **17**, 17471.
41 *Materials Studio 5.0*, Accelrys Software Inc, San Diego, California, USA, 2009.
42 D. M. Többens and S. Zander, *Journal of Large-Scale Research Facilities*, 2016, **2**, A49.
43 A. Schneemann, V. Bon, I. Schwedler, I. Senkovska, S. Kaskel and R. A. Fischer, *Chem. Soc. Rev.*, 2014, **43**, 6062.
44 M. Wojdyr, *J. Appl. Crystallogr.*, 2010, **43**, 1126.
45 J. VandeVondele, M. Krack, F. Mohamed, M. Parrinello, T. Chassaing and J. Hutter, *Comput. Phys. Commun.*, 2005, **167**, 103.
46 G. Lippert, J. Hutter and M. Parrinello, *Mol. Phys.*, 1997, **92**, 477.
47 J. P. Perdew, K. Burke and M. Ernzerhof, *Phys. Rev. Lett.*, 1996, **77**, 3865.
48 S. Goedecker, M. Teter and J. Hutter, *Phys. Rev. B*, 1996, **54**, 1703.
49 C. Hartwigsen, S. Goedecker and J. Hutter, *Phys. Rev. B*, 1998, **58**, 3641.
50 M. Krack, *Theor. Chem. Acc.*, 2005, **114**, 145.
51 J. VandeVondele and J. Hutter, *J. Chem. Phys.*, 2003, **118**, 4365.
52 S. Grimme, J. Antony, S. Ehrlich and H. Krieg, *J. Chem. Phys.*, 2010, **132**, 154104.
53 M. Valiev, E. J. Bylaska, N. Govind, K. Kowalski, T. P. Straatsma, H. J. J. Van Dam, D. Wang, J. Nieplocha, E. Apra, T. L. Windus and W. A. de Jong, *Comput. Phys. Commun.*, 2010, **181**, 1477.
54 C. Adamo and V. Barone, *J. Chem. Phys.*, 1999, **110**, 6158.
55 F. Weigend, *Phys. Chem. Chem. Phys.*, 2006, **8**, 1057.
56 P. S. Petkov, V. Bon, C. L. Hobday, A. B. Kuc, P. Melix, S. Kaskel, T. Düren and T. Heine, *Phys. Chem. Chem. Phys.*, 2019, **21**, 674.
57 S. Ehrling, E. M. Reynolds, V. Bon, I. Senkovska, T. E. Gorelik, M. Mendt, M. S. Weiss, A. Poeppl, E. Brunner, U. Kaiser, A. Goodwin and S. Kaskel, *Adaptive Response of a Metal–organic Framework Through Reversible Disorder–disorder Transitions*, 2020, DOI: 10.26434/chemrxiv.12326165.v1.
58 J. E. Mondloch, M. J. Katz, N. Planas, D. Semrouni, L. Gagliardi, J. T. Hupp and O. K. Farha, *Chem. Commun.*, 2014, **50**, 8944.
59 A. J. Howarth, A. W. Peters, N. A. Vermeulen, T. C. Wang, J. T. Hupp and O. K. Farha, *J. Mater. Chem.*, 2017, **29**, 26.
60 A. P. Nelson, O. K. Farha, K. L. Mulfort and J. T. Hupp, *J. Am. Chem. Soc.*, 2009, **131**, 458.
61 E. J. Carrington, C. A. McAnally, A. J. Fletcher, S. P. Thompson, M. Warren and L. Brammer, *Nat. Chem.*, 2017, **9**, 882.
62 J. E. ten Elshof, C. R. Abadal, J. Sekulić, S. R. Chowdhury and D. H. A. Blank, *Microporous Mesoporous Mater.*, 2003, **65**, 197.
63 P. Melix and T. Heine, *J. Phys. Chem. C*, 2020, **124**, 11985.
64 J.-R. Li, R. J. Kuppler and H.-C. Zhou, *Chem. Soc. Rev.*, 2009, **38**, 1477.
65 S. Bureekaew, S. Amirjalayer and R. Schmid, *J. Mater. Chem.*, 2012, **22**, 10249.
66 G. A. Miller and R. B. Bernstein, *J. Phys. Chem.*, 1959, **63**, 710.
67 D. Zahn and J. Anwar, *Chem. – Eur. J.*, 2011, **17**, 11186.
68 A. Krylov, A. Vtyurin, P. Petkov, I. Senkovska, M. Maliuta, V. Bon, T. Heine, S. Kaskel and E. Slyusareva, *Phys. Chem. Chem. Phys.*, 2017, **19**, 32099.
69 S. Ehrling, M. Mendt, I. Senkovska, J. D. Evans, V. Bon, P. Petkov, C. Ehrling, F. Walenszus, A. Pöppl and S. Kaskel, *J. Mater. Chem.*, 2020, **32**, 5670.
70 S. M. J. Rogge, M. Waroquier and V. Van Speybroeck, *Nat. Commun.*, 2019, **10**, 4842.
71 N. Kavoosi, V. Bon, I. Senkovska, S. Krause, C. Atzori, F. Bonino, J. Pallmann, S. Paasch, E. Brunner and S. Kaskel, *Dalton Trans.*, 2017, **46**, 4685–4695.